International Journal of Solids and Structures 45 (2008) 6205–6219

Contents lists available at ScienceDirect

International Journal of Solids and Structures

journal homepage: www.elsevier.com/locate/ijsolstr

Simulations of a top-hat section subjected to axial crushing taking into account material and geometry variations

Ø. Fyllingen *, O.S. Hopperstad, M. Langseth

Structural Impact Laboratory (SIMLab, Centre for Research based Innovation), Department of Structural Engineering, Norwegian University of Science and Technology, Richard Birkelands veg 1a, 7491 Trondheim, Norway

ARTICLE INFO

Article history:
Received 17 March 2008
Received in revised form 12 June 2008
Available online 31 July 2008

Keywords:
Finite element method
Thin-walled section
Geometric imperfections
Material variations

ABSTRACT

Simulations of top-hat thin-walled sections of dual-phase steel DP800 subjected to axial crushing have been performed taking into account process history and measured geometric imperfections, thickness variations and material variations. The simulations were based on experiments performed by Fyllingen et al. [Fyllingen, Ø., Hopperstad, O.S., Langseth, M., 2008. Robustness study on the behaviour of top-hat thin-walled high-strength steel sections subjected to axial crushing. International Journal of Impact Engineering, in press, doi:10.1016/j.ijimpeng.2008.03.005], who investigated the robustness of a top-hat section subjected to axial crushing. The geometry variation and spatial strain hardening variation were mapped onto the model. The fracture parameter and strain-rate sensitivity were based on values obtained from one of the batches. It was emphasised to use an element type, element size, a fracture criterion and a spot-weld model typically used by the industry. Compared to nominal models especially the thickness variations, geometric imperfections and material failure criterion influenced the behaviour. The material batch variation resulted in large differences in the batch means of the mean crushing forces and the variation in the geometric imperfections and thickness resulted in variation in the mean crushing force within each batch. Compared to the experiments the model generally under-predicted the mean crushing force.

1. Introduction

In car collisions, most of the energy is dissipated by body deformation. Depending on the type of collision, members are loaded axially and by bending or a combination thereof. Axially loaded members will normally dissipate a substantial part of the energy during a front collision. Large scatter in the dissipated energy may be observed for such members, which normally collapse by folding and bending of the plate elements composing the component. Small variations in geometry, material properties as well as boundary and loading conditions can produce this scatter in the results. A non-robust behaviour may lead to a reduced energy dissipation and thus cause increased accelerations and intrusions in the compartment.

The automotive industry emphasises robust behaviour of the energy-dissipating structures. Hence, the structures should behave well even if there are variations in the material, geometry, loading and boundary conditions. In order to reduce the lead time to develop a new product and the cost, the automotive industry uses finite element analysis. Accurate description of the material behaviour, geometry, process history and boundary conditions may be necessary in order to obtain reliable results from such simulations.

* Corresponding author. Tel.: +47 73 59 47 00; fax: +47 73 59 47 01.
E-mail address: orjan.fyllingen@ntnu.no (Ø. Fyllingen).

0020-7683/$ - see front matter © 2008 Elsevier Ltd. All rights reserved.
doi:10.1016/j.ijsolstr.2008.07.011

In the present study the effect of taking into account process history, material variation and geometric imperfections in simulations of axial crushing of a top-hat section will be investigated and compared to experimental results. The model is based on measurements and experiments performed by Fyllingen et al. (2008), who examined variation in the behaviour of a spot-welded top-hat section of DP800 subjected to axial crushing. It was emphasised to use an element type, element size and spot-weld model typically used by the automotive industry.

A review of literature showed that quite a few articles have been published on axial crushing of top-hat steel sections (e.g. Omar et al. (1996), White et al. (1999), White and Jones (1999a,b,c), Schneider and Jones (2004), Peixinho et al. (2003), Yamashita et al. (2003), Schneider and Jones (2004), Tarigopula et al. (2006)). The novelty of this paper compared to the investigations found in the literature, is to investigate the influence of measured in-homogeneities mapped onto the finite element model.

2. Constitutive model and parameter identification

The material used in the components was the dual-phase steel Dogal DP800 produced by the Swedish steel works SSAB Tunnplåt AB. In order to characterise the properties of this material an extensive testing program has been carried out by Tarigopula et al. (2008), Eriksson et al. (2007) and Fyllingen et al. (2008). Tarigopula et al. (2008) investigated the strain-rate sensitivity of DP800, while Eriksson et al. (2007) calibrated a material model for use in large scale finite element analysis that includes plastic anisotropy and failure. In the study carried out by Fyllingen et al. (2008), the variation of material properties within and between the batches was characterised by use of tensile tests. The choice of constitutive model was based on the experiences gained in the abovementioned investigations.

2.1. Constitutive model

Eriksson et al. (2007) performed tensile tests with orientations 0°, 45° and 90° to the rolling direction. From these tests they found that the material exhibits a weak anisotropy in the plastic flow in terms of the Lankford coefficient (width-to-thickness incremental plastic strains). In the present study the weak anisotropy is neglected, and consequently the material is modelled by use of an isotropic yield criterion. A high exponent yield criterion is adopted (Hershey and Dahlegren, 1954), where under the plane stress assumption the effective stress $\bar{\sigma}$ is expressed as

$$\bar{\sigma} = \left[\frac{1}{2}\left\{|\sigma_1|^m + |\sigma_2|^m + |\sigma_1 - \sigma_2|^m\right\}\right]^{\frac{1}{m}} \tag{1}$$

where (σ_1,σ_2) are the principal stresses in the plane of the sheet. According to Logan and Hosford (1980) the exponent m is typically 6 for bcc materials. The material is a dual-phase steel, but however it was chosen to use an exponent m equal to 6. Further, associated flow and isotropic work hardening are assumed. The following non-linear strain hardening function is chosen:

$$\sigma_Y(\bar{\varepsilon}) = \alpha_1 + \alpha_2(\beta + \bar{\varepsilon})^{\alpha_3} \tag{2}$$

Here, σ_Y is the flow stress, $\bar{\varepsilon}$ is the effective plastic strain, and $(\alpha_1, \alpha_2, \alpha_3)$ and β are fitting parameters determined from standard tensile tests. This strain hardening function was chosen for several reasons which will be explained in Section 2.2. The strain-rate dependency of DP800 was investigated by Tarigopula et al. (2008) and it was proposed to take into account the strain-rate dependency by the constitutive relation:

$$\bar{\sigma} = \sigma_Y\left(1 + \frac{\dot{\bar{\varepsilon}}}{\dot{\varepsilon}_0}\right)^q \tag{3}$$

where $\dot{\bar{\varepsilon}}$ is the effective plastic strain-rate, and $\dot{\varepsilon}_0$ and q are material parameters.

Eriksson et al. (2007) argued that at least three different failure-related phenomena should be represented and characterised for DP800: thinning instability, ductile fracture and through-thickness shear instability. It was proposed that for large-scale simulations the criterion developed by Cockroft and Latham (1968) could represent ductile fracture. The Cockcroft–Latham (C–L) criterion for workability reads:

$$W = \int_0^{\bar{\varepsilon}} \langle\hat{\sigma}_1\rangle d\bar{\varepsilon} \geqslant W_c \Rightarrow \text{ fracture} \tag{4}$$

where W is the Cockcroft–Latham integral, W_c is a material parameter and $\langle\cdots\rangle$ is the Macauley bracket.

The model was implemented as a user-defined model in LS-DYNA and is similar to the model described by Reyes et al. (2006). The main differences between the models are the strain hardening given in Eq. (2) and the possibility of assigning each element different values of $(\alpha_1, \alpha_2, \alpha_3)$ and β. In addition, several of the features provided in the model described by Reyes et al. (2006) were excluded, such as plastic anisotropy and kinematic hardening.

2.2. Identification of material parameters

As mentioned, several studies on the material behaviour of DP800 have been performed previously. The results from these investigations will be used to identify the material parameters for the model presented in Section 2.1.

Fyllingen et al. (2008) investigated how the material properties change within and between different batches. A short summary of the study is given here. Materials from five different coils from five different batches were investigated. The coils were named C1, C2, C3, C4 and C6, see Fig. 1 (a).

From C1, C2, C4 and C6 one row of material tests were taken out as depicted in Fig. 2 (a). The specimens, starting with the leftmost were called S1, S2, ..., S*N*, where *N* is the total number of specimens for the sheet in consideration. Three sheets were taken out from C3 and named C3A, C3B and C3C, see Fig. 1 (a). From each of these sheets material specimens were cut out as shown in Fig. 2 (b). All the specimens had the geometry given in Fig. 1 (b). The tensile tests were performed at room temperature under displacement control with a constant displacement rate of 10 mm/min. The deformation of the specimen was measured by use of an extensometer with a gauge length of 80 mm. The material properties varied within each batch and a certain batch-to-batch variation was found. A higher ductility in terms of the ultimate strain was negatively correlated to the ultimate strength and the 0.2% proof strength.

For each test the true stress, σ, true strain, ε, and true plastic strain, ε_p, may be found by use of the formulas:

$$\sigma = s(1+e); \quad \varepsilon = \ln(1+e); \quad \varepsilon_p = \varepsilon - \frac{\sigma}{E} \tag{5}$$

where s is the engineering stress, e is the engineering strain and E is Young's modulus. A strain hardening curve, σ_Y may be fitted to the data by use of a least square fit:

$$\min(f), \quad f = \sum_{i=1}^{N} \left[\sigma^i - \sigma_Y(\varepsilon_p^i)\right]^2 \tag{6}$$

where f is the function to be minimised, N is the number of data points, and σ^i and ε_p^i are the true stress and true plastic strain at point i, respectively. The strains were discretized into 1000 equidistant points from $\varepsilon_p = 0.002$ to $\varepsilon_p(s_u)$, where $\varepsilon_p(s_u)$ is the true plastic strain at the maximum engineering stress (s_u). The stresses at the discretized strains were found by linear interpolation of the experimental data. Several of the common parametric functions for σ_Y were tested, such as the Voce law, Ludwik's law and Swift's law. Especially the Ludwik's law (equal to Eq. (2) with $\beta = 0$) gave a very good fit to the experimental data. However, the initial yield stress, $\sigma_Y(0)$, was negative for the curves from some of the batches, which is unacceptable. By constraining the initial yield stress, the function f increased drastically. Hence, it was decided to constrain the initial yield stress by introducing an initial strain β in the following way:

$$\beta = \begin{cases} \left(\frac{a-\alpha_1}{\alpha_2}\right)^{\frac{1}{\alpha_3}}, \alpha_1 < a \\ 0, \alpha_1 \geqslant a \end{cases} \tag{7}$$

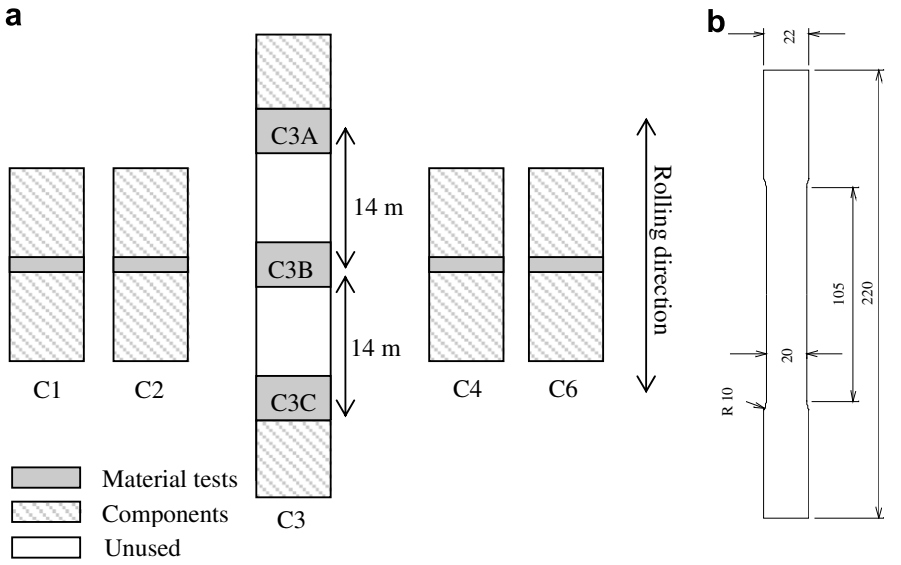

Fig. 1. (a) Schematic view of the position of sheets for material tests (shaded area), components (line shaded area) and rest material (white). (b) The geometry of the tensile specimen (in mm) (adopted from Fyllingen et al., 2008).

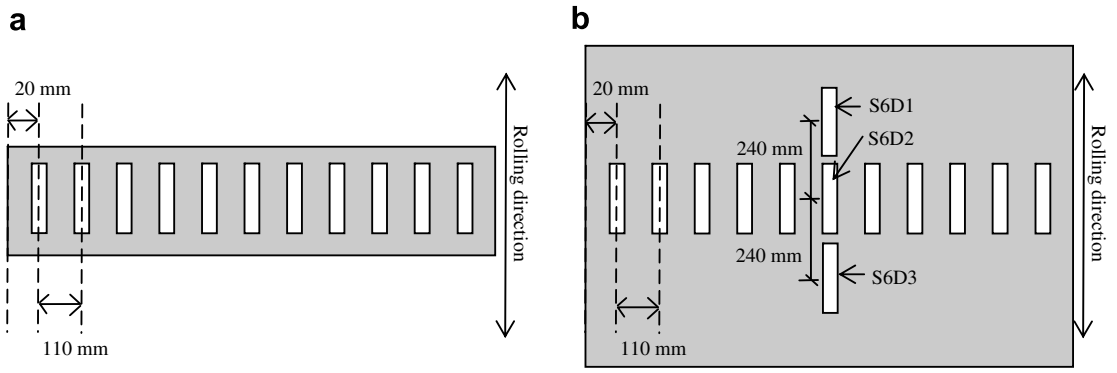

Fig. 2. Schematic view of the position of tensile specimens; (a) for C1, C2, C4 and C6; (b) for C3A, C3B and C3C (adopted from Fyllingen et al., 2008).

Hence, the initial yield stress σ_0 is ensured to be larger than or equal to a. For DP800 there is no obvious point of initial yielding. At least the value of a should be larger than 0 MPa and lower than the 0.2% proof stress. It was chosen to set a equal to 400 MPa. Fits were done for the curves obtained from the rows of specimens from C1, C2, C3B, C4 and C6. In Fig. 3 (a) the square root of the minimum of the function f divided by N is presented for all the specimens. The fits are in general quite good. A comparison between the fitted curve and the experimental curve for a specimen called C4S5, which had the maximum value of f, is demonstrated in Fig. 3 (b). The fitted curve (fit) seems to represent the experimental curve (exp) very well.

An evaluation on how well the model describes the material variation across each sheet is carried out next. For each sheet, the variations of the stresses at certain strain levels are plotted in Fig. 4. The following strain levels were chosen; 0.002, 0.022, 0.042, 0.062 and 0.082. In the figure the x-axis is the position of the specimens, where the origin is placed at the centre of the sheets. The experimental values are drawn with solid lines, while dotted lines are used for the values found from the model. Linear interpolation were used in-between the data points. From Fig. 4 it seems like the variation across the sheets is adequately described.

The observed material variations are transferred to the finite element environment in the following way. The stress at a certain strain level is linearly interpolated in-between the data points across the plate. Since $\varepsilon_p(s_u)$ varies across the sheets, the fitting will be done up to the minimum $\varepsilon_p(s_u)$ of the sheet in consideration. The values of the strain hardening parameters for an element j with its midpoint at position x_j, will be determined by use of Eq. (6) with the interpolated stresses found at x_j.

An average stress–strain curve for each coil is established by averaging the stress across each coil at certain strain levels. In Table 1 average hardening parameters for each coil are presented. The parameters for a coil were found by fitting the hardening model to the average stress–strain curve.

The strain-rate sensitivity for C3 was investigated by Tarigopula et al. (2008). In Fig. 5 the true stresses at a plastic strain of 0.08 are plotted versus the plastic strain-rate. The dotted line is the model with $\dot{\varepsilon}_0 = 0.261\ s^{-1}$ and $q = 0.0138$, which is in good agreement with the experimental data (dots). Since data about the strain-rate sensitivity was not available for the other coils, it will be assumed that the strain-rate sensitivity parameters are constant.

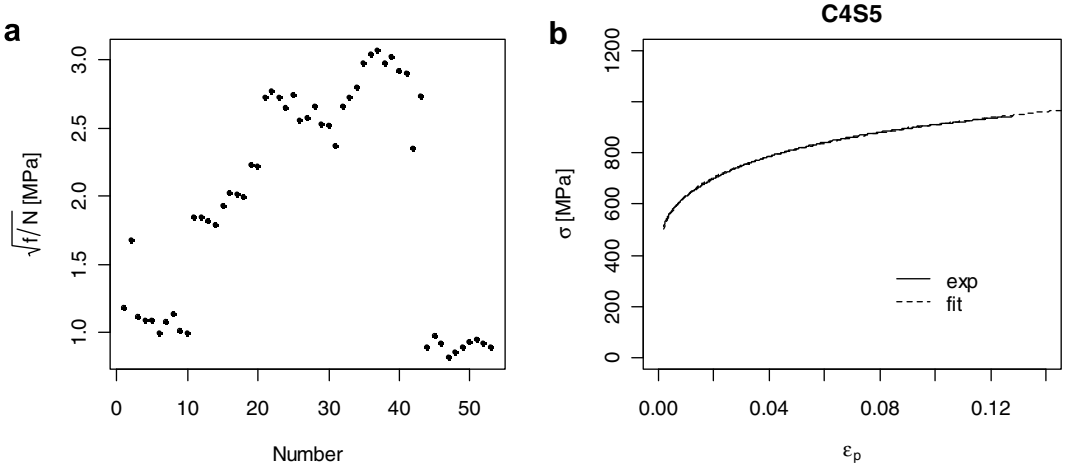

Fig. 3. Original model (a) fitting error; (b) comparison between experimental and fitted stress–strain curves for C4S5.

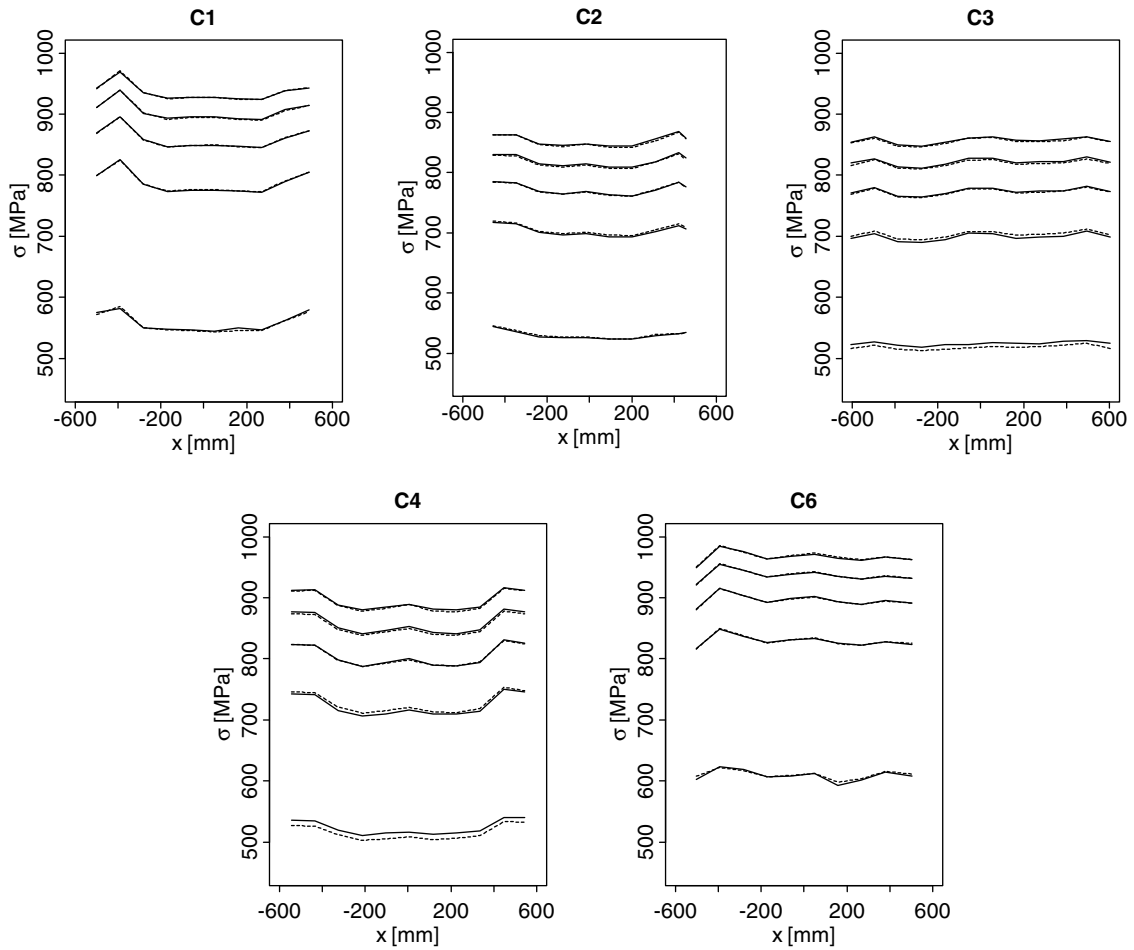

Fig. 4. Comparison of stresses from experiments and model at different strain levels.

Table 1
Material parameters for mean curve of each coil

Coil	α_1 (Mpa)	α_2 (Mpa)	α_3	β
C1	−1489.1	2736.6	0.04845	0.00047624
C2	296.9	996.4	0.23369	0.00006079
C3	238.3	1062.1	0.21715	0.00017191
C4	89.0	1257.1	0.17857	0.00040089
C6	−782.2	2047.0	0.06279	0.00015935

Tarigopula et al. (in press) have calibrated the Cockcroft–Latham fracture criterion for C3 by use of inverse modelling of in-plane shear tests. Based on shell element simulation it was found that W_c should be about 590 MPa. Since no data was available for the other coils it will be assumed that W_c is constant.

In the shear tests large plastic strains are obtained without strain localisation. By simulation of the shear tests with the material model proposed in Section 2.1 and hardening parameters fitted to the tensile test experiments performed by Tarigopula et al. (in press), a very good correlation between the model and the experimental results was obtained. Hence, the hardening model seems to give a reasonable extrapolation of the hardening curve beyond necking. However, this was only done for C3, and thus the accuracy of the hardening model for large strains for the other coils is uncertain.

2.3. Spot-weld resistance

It has been chosen to adopt a commonly used model already implemented in the finite element code LS-DYNA. In LS-DYNA there exists a model for spot-welds which is called constrained spot-weld. The spot-weld is modelled as a massless

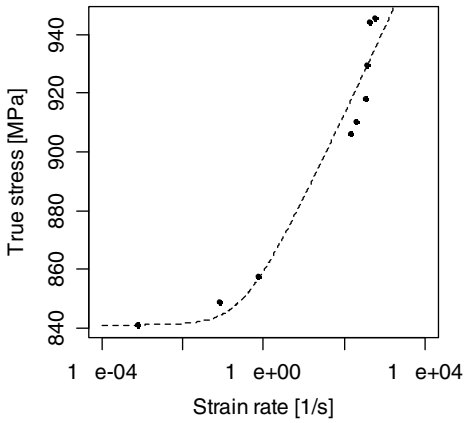

Fig. 5. Strain-rate sensitivity, stress at 0.08 plastic strain versus strain-rate (model – dotted line).

rigid beam, which connects nodal points of nodal pairs; thus, nodal rotations and displacement are coupled. Failure of the spot-welds occurs when

$$\left(\frac{|f_n|}{S_n}\right)^n + \left(\frac{|f_s|}{S_s}\right)^m \geqslant 1 \tag{8}$$

where f_n and f_s are the normal and shear interface forces, S_n is capacity for normal force only and S_s is the capacity for shear force only at spot-weld failure and n and m are exponents for normal and shear force (LS-DYNA Keyword User's Manual, 2007).

Based on experiments by the manufacturer SSAB, S_n and S_s were set equal to 9.4 kN and 15.0 kN, respectively. There was not sufficient data in order to determine the exponents n and m. It was assumed that both exponents were equal to 2, which is within typically values found in the literature (e.g. Lin et al. (2002)).

3. Finite element model

The modelling was divided into several steps taking into account different effects such as the forming process, mapping of geometric deviations and material variations. Before the modelling is explained a short summary of the production process, measurements and experimental set-up will be given. Details may be found in Fyllingen et al. (2008). All the simulations presented here have been performed with the explicit solver in the FEM-code LS-DYNA.

3.1. Production, measurements and experimental set-up

Each component was produced from two sheets with nominal thicknesses of 1.5 mm. The nominal geometry of the top-hat sheet and bottom sheet was 229 mm by 400 mm and 115 mm by 400 mm, respectively. The geometry of the top-hat was achieved by inserting the top-hat sheet in-between the die and punch depicted in Fig. 6 (b). As the punch moved downwards, the corner with an inner radius of 2.0 mm was achieved. The two parts of the top-hat were joined by spot-welding along the centre line of the flange width with a constant weld pitch of 30 mm and a spot-weld diameter of approximately 5 mm. The distance from the free end to the first spot weld was 15 mm. Further, an additional spot-weld was placed 15 mm from the fixed end. The nominal geometry of the component is given in Fig. 6 (a).

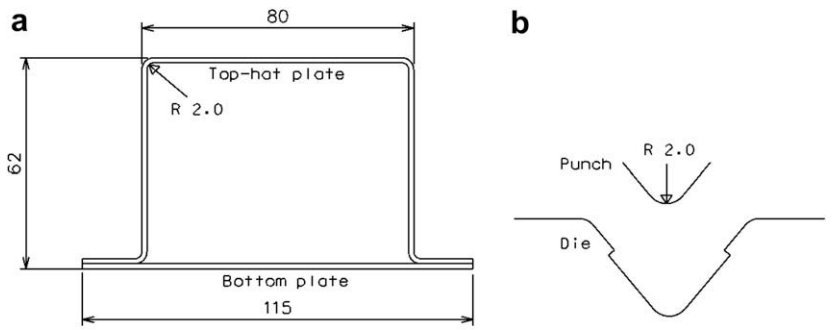

Fig. 6. (a) Cross section of the profile (in mm) and (b) cross section of punch and die (in mm) (adopted from Fyllingen et al., 2008).

Several measurements were carried out during and after the production. The thickness was measured at eight locations on the top-hat sheet and four locations on the bottom sheet, see Fig. 7 (a). The origin is placed at the centre of the sheets, while the *z*-axis and *x*-axis are directed parallel and perpendicular to the rolling direction, respectively. In order to get accurate measurements of the geometry of the top-hat profile an ATOS III 3D scanner was used. A picture of the equipment is given in Fig. 7 (b), where the 3D scanner is located to the upper left in the picture, while the profile lies on a circular table to the lower right. The 3D scanner projects fringe patterns onto the object and by use of two cameras the patterns are captured. By rotating the object on the table, pictures from several directions may be taken and a cloud of points is obtained.

Five components from each of the five coils were tested. The profiles are given a name C*M*P*N*, where *M* is the coil number and *N* is ranging from 1 to 5. The tests were carried out in a pendulum accelerator with a mass of 985 kg impacting the specimen at a velocity of 10 m/s. The pendulum accelerator accelerates a trolley moving horizontally on rails up to a certain velocity towards the specimen. The trolley hits the specimen which is fixed to the reaction wall. By use of a clamping device, 80 mm of the specimen was fixed, and consequently the free length, is 320 mm. A wooden block was inserted into the fixed end of the profiles in order to prevent local buckling of the profile walls inside the clamping device. The trolley was equipped with a load cell to obtain the force, acceleration, velocity and displacement history.

3.2. Model of the bending process

It was decided to take out one strip of material around the corner. The model could be simplified by fixing the longitudinal displacement of the nodes and hence only one row of element was used. The model gave some deviations of the stresses and strains at the ends, but seemed to represent the stresses and strains quite well in-between the ends. In order to avoid the springback simulations only the effective plastic strain and *W* was mapped onto the component. A figure of the model in the initial position and final position is demonstrated in Fig. 8. The strip of material had a length of 20 mm and consisted of 40 elements. It was chosen to use fully integrated elements with five integration points through the thickness.

3.3. Model of the component

FEM-simulations of impacts are quite time consuming. Thus considerations have to be made about what simplifications can be done in order to reduce the CPU-time. Several simulations were carried out initially in order to evaluate the effect of different elements, the number of integration points through the thickness and the mesh density. A mesh with Belytschko-Tsay (type 2) shell elements, five integration points through the thickness and an element size of 3 mm × 3 mm and three

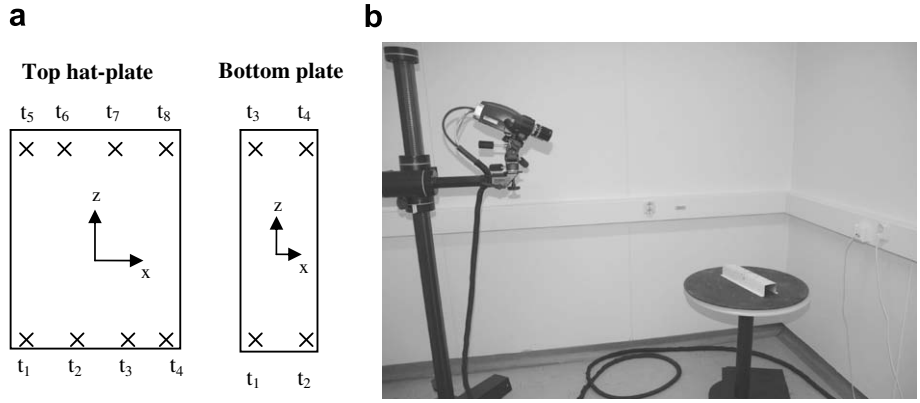

Fig. 7. (a) Thickness measurements of sheets and (b) measurements by use of a 3D scanner (adopted from Fyllingen et al., 2008).

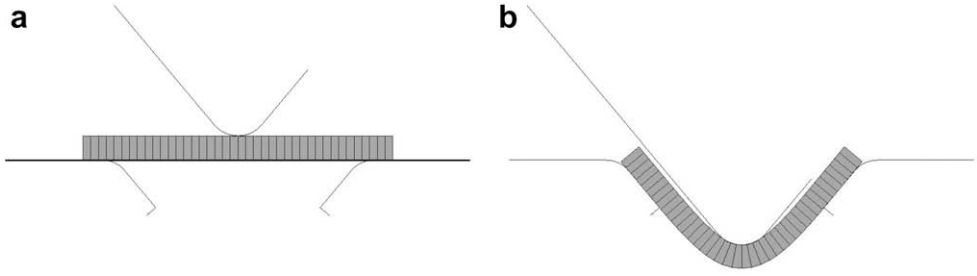

Fig. 8. Forming simulation: (a) initial position and (b) final position.

elements across the arcs gave satisfactory result when fracture was ignored. However, the initiation and evolution of fracture was very mesh dependent. As mentioned, the spot-welds were modelled by use of the constrained spot-weld option in LS-DYNA. Elements were deleted if the Cockcroft–Latham fracture criterion was satisfied in three of the five integration points.

The density was set to 7800 kg/m^3, the Young's modulus was 205,000 MPa and the Poisson's ratio was 0.3. To account for contact between the impactor and the profile, single surface contact algorithm was used, while the self contact was modelled by use of automatic surface to surface contact algorithm. The friction coefficient was set to 0.3 in order to allow sliding movement.

The impactor was modelled as a 300 mm $\times$ 300 mm plate of shell elements with a thickness of 1.5 mm and rigid body material. At the clamped part of the member, which is 80 mm, all degrees of freedom were constrained except longitudinal translation degree of freedom in order to allow deformation in the axial direction. The lower end of the specimen was fixed by constraining all six degrees of freedom.

3.4. Mapping of geometry and history variables from the forming process

As mentioned the outer surface of all the components were measured by use of a 3D scanner. The top-hat and bottom sheet were measured separately resulting in two clouds of points. By use of a script the measured points were related to the finite element model. The thicknesses were measured at eight locations on the top-hat sheet and at four locations at the bottom sheet. It was chosen to use bilinear interpolation to find the thickness at each node. The mapping of the effective plastic strain and W (defined through Eq. (4)) from the forming simulation was done by use of a script since the element type and the mesh density differed and only one corner was simulated.

4. Numerical studies

The numerical studies have been divided into three parts. In the first part, the influence of the geometric imperfections, spot-weld failure and the mapping of history variables from the forming simulations will be investigated, while in the second part the influence of material variation and random spot-weld locations will be investigated. In the third part, simulations of all the components will be done in order to see how the measured geometric imperfections and material variation influence the behaviour and if the experimental variation within and between the batches in the mean force and deformation modes can be captured.

A simulation of the nominal model runs for about 15 h, while the geometric mapping might lead to smaller elements in the corners in some cases leading to an increased simulation time. In order to keep the simulation time to about 15 h it was decided to set a minimum time step equal to the minimum time step of the nominal model. Then LS-DYNA scales the mass of an element if and only if it is necessary to meet the Courant time step size criterion. Hence, the smallest elements in some of the simulations were slightly mass scaled.

4.1. Effect of geometric imperfection, failure and process history

The influence of geometric imperfections, failure and process history will be investigated for two profiles from coils with different behaviour in terms of the amount of fracture. The profiles from C3 experienced a small amount of fracture, while the profiles from C6 experienced a large amount of fracture. From these coils profile C3P5 and C6P2 were chosen. The influence of the different effects will be investigated by adding effects to the nominal model, which is based on the nominal geometry depicted in Fig. 6 (a) and has a thickness equal to 1.5 mm.

In Table 2 the mean crushing force up to 180 mm, P_{180}, is presented for 11 different combinations for both C3P5 and C6P2. In the first five columns it is indicated whether the forming process (form), geometric imperfections (geo), thickness varia-

Table 2
Influence of different effects on the mean crushing force

Effects					P_{180} (kN)	
Form	Geo	Thick	wc	sptw	C3P5	C6P2
0	0	0	0	0	78.1	93.8
1	0	0	0	0	79.5	92.2
0	1	0	0	0	67.4	81.2
0	0	1	0	0	73.0	88.1
0	0	0	1	0	73.4	83.7
0	0	0	0	1	78.1	92.9
1	0	0	1	0	73.9	85.1
1	0	0	0	1	79.3	92.2
1	0	0	1	1	73.9	85.4
1	1	1	0	0	67.0	93.2
1	1	1	1	1	66.5	73.9
Experiments					80.6	74.9
Batch mean of the experiments					77.0	75.3

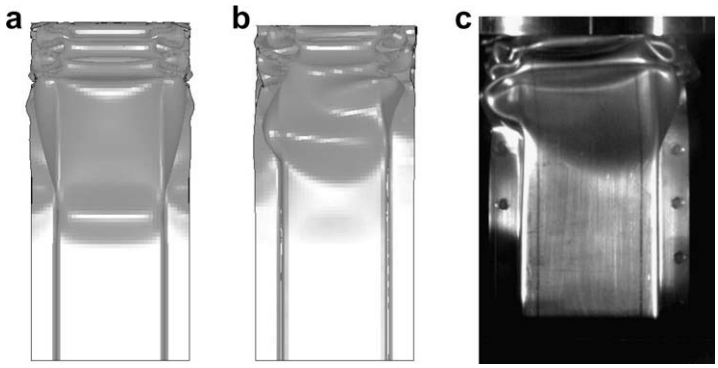

Fig. 9. C3P5 at 0.0168 s: (a) 00000; (b) 11111; (c) experiment.

tion (thick), material fracture (wc) or spot-weld failure (sptw) is included. A (0) indicates that the effect is not included, while a (1) indicates that the effect is included. In the last two rows the experimentally obtained mean crushing force and the batch mean of the experimentally obtained mean crushing force are given.

In the first row of Table 2, the P_{180} for the nominal model is given. It is noticed that P_{180} is remarkably larger for C6P2 than C3P5. The only difference between the two models is the choice of hardening parameters. In the next five rows the influence of each effect is tested. By mapping the history variables from the forming simulations P_{180} is slightly increased, while the introduction of geometric imperfections, thickness variations or material fracture reduces P_{180} substantially. The spot-weld failure is not influencing P_{180} for C3P5, while for C6P2 P_{180} is slightly decreased. In the consecutive rows, P_{180} for combinations of several effects are included. By including history from the forming simulation, the geometric imperfections and thickness variation (combination 11100), P_{180} for C3P5 is almost equal to P_{180} with only geometric imperfections, while P_{180} for C6P2 is remarkably high compared to the influence of each effect. In Figs. 9 and 10 the buckling patterns for several combinations for C3P5 and C6P2 are demonstrated. The buckling pattern between the different simulations for C3P5 differed somewhat, while the buckling patterns for C6P2 differed substantially leading to unexpectedly high mean crushing force for combination 11100. By adding material fracture and spot-weld failure to combination 11100, the mean crushing force drops

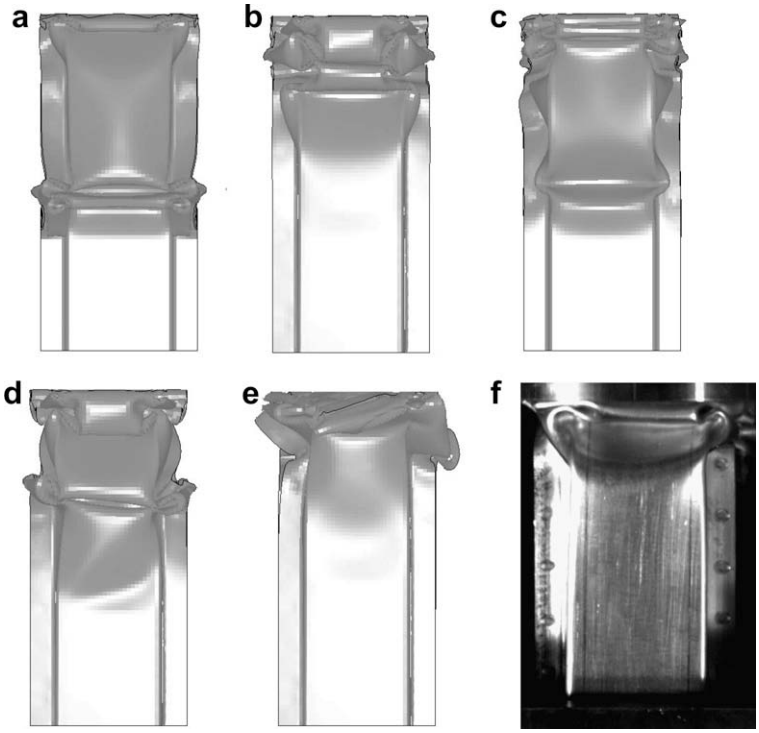

Fig. 10. C6P2 at 0.0168 s: (a) 00000; (b) 01000; (c) 00100; (d) 11100; (e) 11111; (f) experiment.

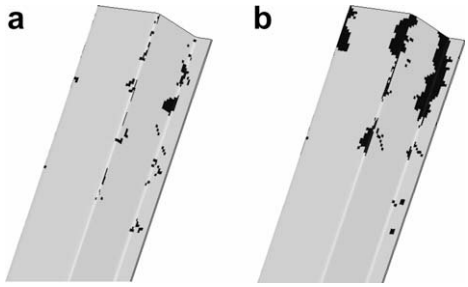

Fig. 11. Deleted elements on un-deformed geometry for 11111 at 0.168 s: (a) C3P5; (b) C6P2.

slightly for C3P5, while it drops quite a lot for C6P2. The amount of deleted elements (black) for the two profiles is demonstrated in Fig. 11. A lot of deleted elements were observed for this combination for C6P2 and the propagation of fracture is certainly unrealistic.

All the force–displacement curves for C3P5 and C6P2 are demonstrated in Fig. 12 (a) and (b). A black solid line is used for the simulations, while a grey solid line is used for the experiments. It is possible to observe large variation in the oscillation patterns between the different combinations.

4.2. Effect of material and spot-weld variation

The influence of material variation and variation of the spot-weld locations will be investigated for C3P5 and C6P2. The exact location of the bottom sheet and top-hat sheet was unknown and could therefore not be directly related to the measured material variations. By testing several different combinations of assumed locations for the sheets it is possible to see if it is likely that material variations might influence the behaviour. The exact positions of the spot-welds for each profile was not measured and hence the effect of assumed variation of the spot-weld location will be investigated.

Each spot-weld was given a deviation in either the longitudinal direction or the transverse direction. It was assumed that the deviations were normally and independently distributed with a standard deviation of 0.5 mm and a mean of 0 mm. In order to avoid large deviations, the distributions were truncated at ±3 standard deviations. By use of Monte-Carlo simulation three samples (sptw 1–3) of each of the two profiles were generated. Two cases from the previous section were selected, namely combination 11100 and 11111. In Table 3 the mean crushing force P_{180} from the simulations is presented. The variation of spot-weld locations leads to small variations in P_{180}. The buckling patterns were only slightly affected by the variation, except for combination C6P2 11111, where differences in the buckling patterns between the three samples were observed.

Concerning the material variation it was chosen to select two positions of the top-hat and bottom sheet called 0 or 1. The top-hat or bottom sheet was cut out from the left edge (1) or at the centre (0) of the sheets, leading to four samples. The samples were named mat ##, where the first and second number corresponds to the position of the top-hat and bottom sheet, respectively. In Table 3 the mean crushing force P_{180} is presented for the combinations 11100 and 11111. Some variation in P_{180} is observed within each of the combinations. The buckling pattern differed slightly within each of the combinations, except for C6P2 11111, where the variation was large. The simulations of C6P2 11111 are depicted in Fig. 13.

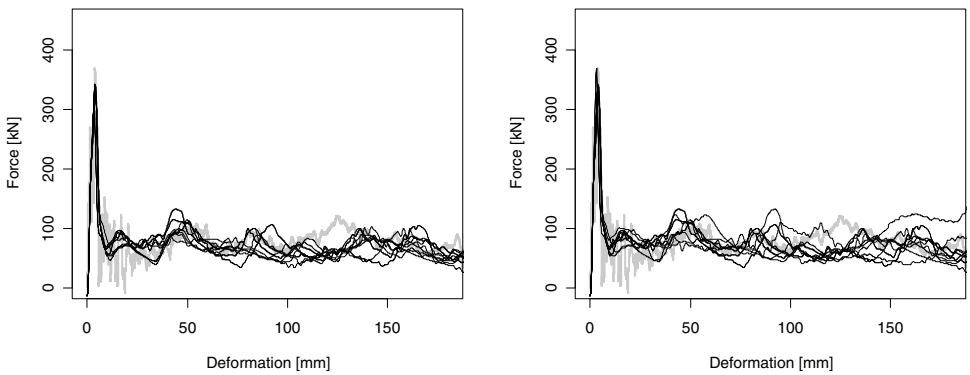

Fig. 12. Force–displacement curves: (a) C3P5; (b) C6P2.

Table 3
Influence of variation in material properties and spot-weld locations

Type	C3P5, P_{180} (kN)		C6P2, P_{180} (kN)	
	11100	11111	11100	11111
sptw 1	67.47	64.40	93.51	75.46
sptw 2	69.55	67.29	92.21	76.88
sptw 3	66.82	66.84	91.15	74.25
mat 00	67.20	67.33	93.05	75.09
mat 01	66.88	67.92	90.53	73.42
mat 10	67.12	67.27	94.44	75.51
mat 11	66.88	67.13	91.62	77.26
No effect	67.04	66.54	93.21	73.86

4.3. Variation in behaviour

The main objective of the experiments performed by Fyllingen et al. (2008) was to investigate the robustness of the top-hat sections. The batch to batch variation in the mean crushing force seemed to be closely related to the material properties, while the reasons for the within-batch variation in the mean crushing force could not be related directly to any of the measurements. One of the possible causes for the within-batch variation is the variation in geometric imperfections. Since the geometry was measured and it is possible to map the measurements onto a finite element model, it can be investigated to what extent the geometric imperfections cause within-batch variation. Since the fracture model does not seem to describe the fracture propagation properly, a combination without fracture and spot-weld failure is included in addition to a model with fracture and spot-weld failure.

In Table 4 the mean crushing force evaluated up to a deformation of 60 mm (P_{60}), 120 mm (P_{120}) and 180 mm (P_{180}) is presented for simulations and experiments of all the profiles. For each batch the mean and standard deviation (Stdev) of the mean crushing force are given. By comparing the mean crushing force from the simulations within each batch there is certainly a within-batch variation, which is caused exclusively by geometric imperfections and thickness variations. Stdev for the models are larger than the experimental Stdev in some cases and smaller in other cases. Also a certain batch-to-batch variation is observed for both models. The model with fracture and spot-weld failure (11111) leads in general to a lower mean crushing force than the model without fracture and spot-weld failure (11100). The difference between the two models is largest for C6 and smallest for C2.

By comparing the batch means of P_{180} obtained in model 11111 to the experimental results, the best agreement is obtained for C6 and C1. For C2, C3 and C4 the batch mean of P_{180} is lower in the simulations than in the experiments for both 11111 and 11100. By comparing the batch mean of P_{60} for both models, the values are higher for C1 and C6 compared to the experiments, while the values are lower for C3. Concerning P_{60} for model 11111 a quite good agreement is observed for especially C2 and a satisfactory agreement is observed for C4.

By comparing the initiation of buckling it was observed that in general the buckling started nearer the fixation for model 11111 than in the experiments. An exception was C3, where the buckles generally initiated nearer the middle of the profile than in the experiments. Concerning the final buckling pattern and extent of fracture for model 11111 there was a good agreement for especially C2. For C4 too much fracture was observed generally, while the agreement varied from some deviations to large deviations for the components in C1, C3 and C6.

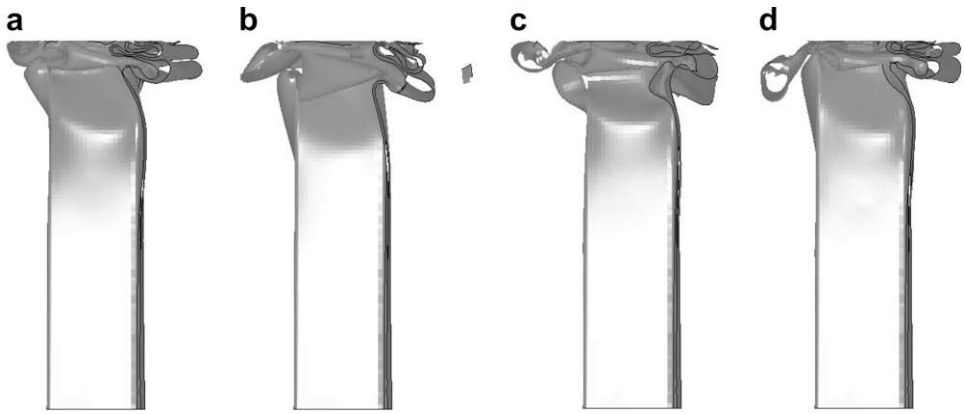

Fig. 13. C6P2 material variation, model 11111 at time 0.168 s: (a) 00; (b) 10; (c) 01; (d) 11.

Table 4
Mean crushing force from simulations and experiments for all the components

Profile	P_{60} (kN)			P_{120} (kN)			P_{180} (kN)		
	11100	11111	Exp	11100	11111	Exp	11100	11111	Exp
C1P1	93.42	86.62	68.31	83.74	82.82	74.73	82.56	75.77	79.25
C1P2	93.28	89.41	80.07	83.46	81.57	85.03	81.37	77.80	82.09
C1P3	93.47	90.56	94.41	83.96	83.30	81.75	81.47	79.59	81.11
C1P4	95.12	90.13	76.29	87.56	78.14	77.26	86.26	71.66	79.53
C1P5	92.38	87.62	85.68	83.49	80.08	83.36	81.24	78.89	78.90
Mean	93.53	88.87	80.95	84.44	81.18	80.43	82.58	76.74	80.17
Stdev	0.99	1.68	9.82	1.75	2.11	4.30	2.12	3.18	1.36
C2P1	78.85	77.29	83.19	69.62	68.54	79.76	67.04	65.31	78.89
C2P2	78.56	77.33	77.80	69.15	67.04	78.32	67.47	63.81	74.33
C2P3	78.71	77.49	79.21	67.82	68.03	71.97	65.75	64.35	71.05
C2P4	85.79	82.18	78.97	72.54	70.91	76.02	70.58	69.82	71.72
C2P5	81.46	80.70	74.36	69.97	68.86	76.37	68.51	66.64	77.94
Mean	80.67	79.00	78.71	69.82	68.67	76.49	67.87	65.99	74.78
Stdev	3.10	2.29	3.17	1.72	1.43	2.94	1.81	2.40	3.55
C3P1	81.21	77.38	85.99	75.84	73.55	83.11	71.74	68.21	78.97
C3P2	82.96	68.68	89.42	75.60	63.02	85.69	73.68	62.32	80.66
C3P3	76.18	74.23	86.18	67.52	63.41	71.67	66.29	64.54	69.32
C3P4	81.14	79.61	79.15	70.89	67.63	77.23	73.23	65.33	75.69
C3P5	78.95	77.50	83.40	69.41	67.49	79.82	67.04	66.54	80.57
Mean	80.09	75.48	84.83	71.85	67.02	79.50	70.40	65.39	77.04
Stdev	2.61	4.26	3.82	3.73	4.25	5.43	3.49	2.21	4.76
C4P1	89.72	80.28	82.77	78.70	72.13	78.30	72.96	66.75	77.48
C4P2	93.16	79.03	86.25	87.53	72.69	81.41	80.30	68.61	80.03
C4P3	92.64	79.06	88.44	88.25	72.58	81.22	77.34	68.19	83.37
C4P4	91.77	84.14	85.40	81.11	74.13	81.12	75.31	71.16	73.46
C4P5	95.68	83.56	83.76	79.88	73.26	83.54	75.77	69.27	79.84
Mean	92.59	81.22	85.32	83.09	72.96	81.12	76.34	68.79	78.84
Stdev	2.17	2.47	2.21	4.47	0.77	1.86	2.71	1.61	3.66
C6P1	110.42	87.48	78.78	100.19	86.19	79.15	94.46	81.98	77.66
C6P2	106.75	84.49	79.26	93.85	83.37	77.59	93.21	73.86	74.87
C6P3	111.26	87.90	91.61	98.13	84.43	72.21	90.97	75.00	71.13
C6P4	108.21	91.20	76.15	90.97	82.06	85.42	84.12	81.37	77.54
C6P5	110.60	86.00	77.04	97.64	82.51	79.27	98.64	81.01	75.40
Mean	109.45	87.41	80.57	96.16	83.71	78.73	92.28	78.64	75.32
Stdev	1.89	2.51	6.30	3.69	1.65	4.72	5.35	3.88	2.65

In Fig. 14 pictures of the final geometry from simulations (model 11111) and experiments, and additionally force–displacement curves are given for profile C2P5, C6P1 and C1P3. It may be observed that there are some deviations between the simulations and experiments in the buckling pattern. Some of the simulations were in better agreement with the experiments, while the major part of the simulations had from some to large deviations in the buckling and fracture pattern.

5. Discussion

The objective with the present study was to investigate the influence of taking into account process history, measured variations in geometric imperfections, thickness and material properties in finite element simulations of a top-hat profile of DP800 subjected to axial crushing and to compare the simulations to the experiments. It was chosen to use a finite element model with an element type, element size and spot-weld model which is typically used by the automotive industry.

Detailed measurements of the geometry, thickness and material variations have been performed previously by Fyllingen et al. (2008). However, there was only data for the fracture model and strain-rate sensitivity from one of the batches. Hence, the possible batch-to-batch variations of these parameters were neglected in the present study.

Based on the study performed in Section 4.1 there is certainly an effect of several of the factors compared to a nominal model. Especially the thickness variation, the geometry variation and the fracture model influence the results when applied once at the time. Because the behaviour of the profiles seems to be very sensitive to small changes, applying several factors at the time may result in a change in the buckling mode which in one case led to unexpended results regarding the mean crushing force. For crash members the industry quite usually use geometrical triggers to control the behaviour and to control the energy absorption. However, a geometrical trigger was not used in the experimental study (Fyllingen et al., 2008) since the

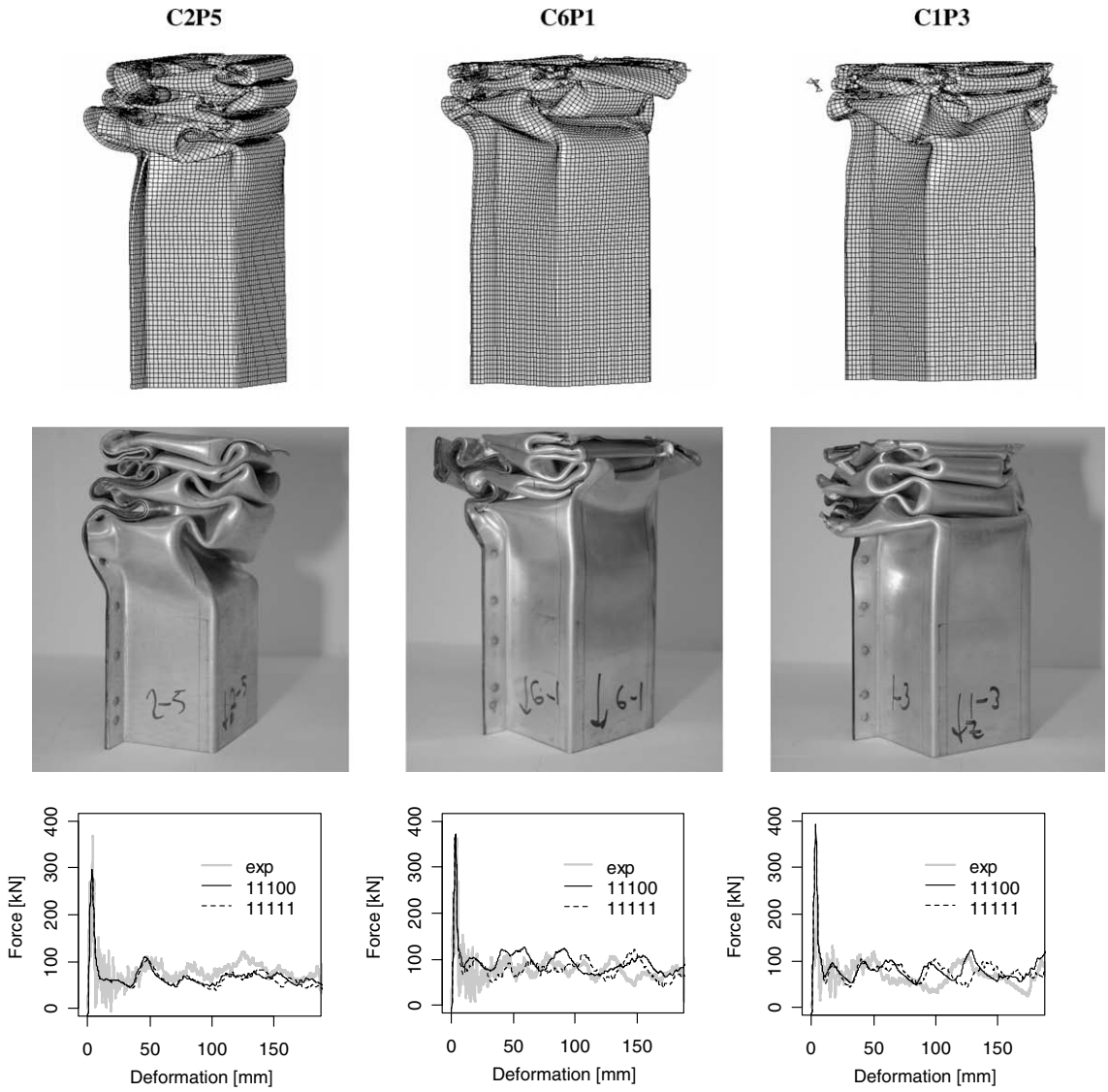

Fig. 14. Comparison experiments and simulations for profile C2P5, C6P1 and C1P3.

effect of the geometrical imperfections then could vanish. Regarding the fracture model, the propagation of fracture seemed to be unrealistic. However, the amount of fracture is much larger for component C6P2 than for component C3P5 and the effect of adding fracture and spot-weld failure to the model of C6P2 was much larger than adding the effects to the model of C3P5. This is in agreement with experimental trends.

In Section 4.2 the effects of spot-weld positions and material variation were investigated. Since the exact position of the plates composing the component and the position of the spot-welds were not measured, assumptions about the positions were made. Both the random positioning of the spot-welds and the material variation resulted in some variation in the mean crushing force, which might be important in order to get the correct variance. However, it should be mentioned that the model of the spot-weld is very simple and by use of more advanced models the results might differ.

An overall comparison of the experiments and simulations performed in Section 4.3 is given in Fig. 15. The batch mean of the mean crushing force evaluated up to 180 mm is given as well as the mean plus/minus one standard deviation. For C2, C3 and C4 a smaller amount of fracture was observed in the experiments. Hence, model 11100 is expected to give reasonable results. In the left diagram in Fig. 15, it is observed that for C2, C3 and C4 the mean crushing force is under-predicted by use of model 11100. By including fracture and spot-weld failure the force level drops even further, resulting in an even larger under-prediction of the mean crushing force for these coils. For C1 and especially C6 larger amount of fracture were observed and hence it was expected that the mean crushing force should be over-predicted for model 11100. This was also observed, and by including fracture and spot-weld failure the mean crushing force drops. However, the fracture patterns were not real-

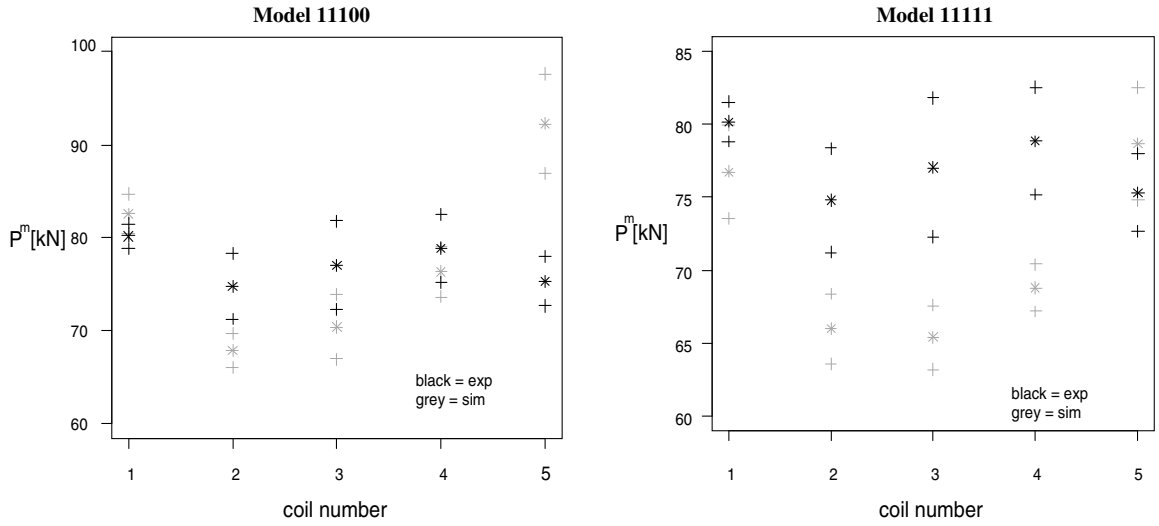

Fig. 15. Comparison of the mean crushing force obtained in experiments and simulations (* = batch mean, + = batch mean ± one batch standard deviation.)

istic and hence it is not possible to say that a good correlation was obtained. Based on the abovementioned observations it is believed that the model in general under-predicts the mean crushing force and that the fracture model or its calibration is not fully appropriate for describing the evolution of fracture.

6. Concluding remarks

The objective with the present study was to investigate the influence of taking into account process history, measured variations in geometric imperfections, thickness and material properties in finite element simulations of a top-hat profile of DP800 subjected to axial crushing and to compare the simulations to the experiments. It was chosen to use a finite element model with an element type, element size and spot-weld model, which is typically used by the automotive industry. However, the parameters for the fracture model and strain-rate hardening were obtained from material tests from one batch only. Further, the small anisotropy was neglected.

The numerical studies were divided into three parts. In the first part models taking into account the process history, measured geometric imperfections, measured thickness, material fracture and spot-weld failure were compared to a nominal model for two profiles. Compared to the nominal models, the effect of the geometric imperfections was largest, while the effect of the forming operation and spot-weld failure were smaller. From this part it may be concluded that especially the thickness variations, geometric imperfections and material failure criterion influence the behaviour. By comparing the two nominal models, the material properties from two different batches certainly influence the mean crushing force.

In the second, part it was found that the variation in the mean crushing force caused by variations of material properties and spot-weld locations resulted in some variation. Hence, these variations should be included in simulations in order to have accurate results. However, detailed measurements were not done in the current study and thus a direct comparison to the experimental results was not done.

In the last part, the influence of material batch variation, variation in geometrical imperfections and spatial thickness variation was investigated and compared to experiments. Since the fracture model did not describe the fracture propagation properly, a model without fracture and spot-weld failure was included in addition to a model with fracture and spot-weld failure. Variations of geometric imperfections and spatial thickness resulted in variations in the mean crushing force and the buckling pattern. There was a certain batch-to-batch variation in the mean crushing force and this was closely related to the material properties. It is believed that the model in general under-predicts the mean crushing force and that the fracture model or its calibration is not appropriate for describing the evolution of fracture.

From this study it may be concluded that taking into account variation in material properties, geometric imperfections and thickness variations in simulations certainly influence the results for the considered top-hat profile. The model presented here seems to capture some of the variations found in the experiments, but further improvement is necessary in order to have more predictable results.

Acknowledgement

The present work has been carried out with financial support from The Norwegian University of Science and Technology and the BIP project ROBDES. The ROBDES project is founded by the Research Council of Norway, Hydro Aluminium Structures, Volvo Car Corporation, Ford, Scania, SSAB Tunnplåt and Gestamp Hardtech.

References

Cockroft, M.G., Latham, D.J., 1968. Ductility and the workability of metals. Journal of the Institute of Metals 96, 33–39.

Eriksson, M., Lademo, O.-G., Hopperstad, O.S., Langseth, M., 2007. Deterministic material modelling for forming and crash analyses of metal components. A procedure for material modelling and characterisation, with focus on formability and failure. SINTEF REPORT STF80MK F06314.

Fyllingen, Ø., Hopperstad, O.S., Langseth, M., 2008. Robustness study on the behaviour of top-hat thin-walled high-strength steel sections subjected to axial crushing. International Journal of Impact Engineering, in press, doi:10.1016/j.ijimpeng.2008.03.005.

Hershey, A.V., Dahlegren, V.A., 1954. The plasticity of an isotropic aggregate of anisotropic face-centred cubic crystals. American Society of Mechanical Engineers – Transactions – Journal of Applied Mechanics 21 (3), 241–249.

Lin, S.-H., Pan, J., Wu, S.-R., Tyan, T., Wung, P., 2002. Failure loads of spot welds under combined opening and shear static loading conditions. International Journal of Solids and Structures 39, 19–39.

Logan, R.W., Hosford, W.F., 1980. Upper-bound anisotropic yield locus calculations assuming ⟨1 1 1⟩ – pencil glide. International Journal of Mechanical Science 22, 419–430.

LS-DYNA Keyword User's Manual, 2007. Version 971, Livermore Software Technology Corporation.

Omar, T.A., Kan, C.-D., Bedewi, N.E., 1996. Crush behaviour of spot welded hat section components with material comparison. Proceeding of Crashworthiness and Occupant Protection in Transportation Systems ASME, AMD 218, 65–78.

Peixinho, N., Jones, N., Pinho, A., 2003. Experimental and numerical study in axial crushing of thin walled sections made of high strength steels. Journal of Physics IV France 110, 717–722.

Reyes, A., Hopperstad, O.S., Lademo, O.-G., Langseth, M., 2006. Modeling of textured aluminum alloys used in a bumper system: material tests and characterization. Computational Materials Science 37, 246–268.

Schneider, F., Jones, N., 2004. Impact of thin-walled high-strength steel structural sections. Proceedings of the Institute Mechanical Engineering, Part D: Journal of Automobile Engineering 218 (2), 131–158.

Tarigopula, V., Langseth, M., Hopperstad, O.S., Clausen, A.H., 2006. Axial crushing of thin-walled high-strength steel sections. International Journal of Impact Engineering 32, 847–882.

Tarigopula, V., Hopperstad, O.S., Langseth, M., Clausen, A.H., Hild, F., 2008. A study of localisation in dual-phase high-strength steels under dynamic loading using digital image correlation and FE analysis. International Journal of Solids and Structures 45, 601–619.

Tarigopula, V., Hopperstad, O.S., Langseth, M., Clausen, A.H., Hild, F., Lademo, O.-G., Eriksson, M., in press. A study of large plastic deformations in dual phase steel using digital image correlation and FE analysis. Experimental Mechanics, doi:10.1007/s11340-007-9066-4.

White, M.D., Jones, N., 1999a. A theoretical analysis for dynamic crushing of top-hat and double-hat thin-walled sections. Proceedings of the Institution of Mechanical Engineers, Part D: Journal of Automobile Engineering 213 (4), 307–325.

White, M.D., Jones, N., 1999b. Experimental study into the energy absorbing characteristics of top-hat and double-hat sections subjected to dynamic axial crushing. Proceedings of the Institution of Mechanical Engineers, Part D: Journal of Automobile Engineering 213 (3), 259–278.

White, M.D., Jones, N., 1999c. Experimental quasi-static axial crushing of top-hat and double-hat thin-walled sections. International Journal of Mechanical Sciences 41, 179–208.

White, M.D., Jones, N., Abramowicz, W., 1999. A theoretical analysis for the quasi-static axial crushing of top-hat and double-hat thin-walled sections. International Journal of Mechanical Sciences 41, 209–213.

Yamashita, M., Gotoh, M., Sawairi, Y., 2003. A numerical simulation of axial crushing of tubular strengthening structures with various hat-shaped cross-sections of various materials. Key Engineering Materials, 193–198.